Semi-quantification of the minimum detectable difference of imaging quality of gamma camera SPET for four radionuclides via an innovative PMMA phantom with a V-shaped slit: interpretation of a feasibility study

Chih-Feng Chang[1,2] MD,
Chih-Feng Chen[3] DVM,
Tzu-Hwei Wang[4,5] MD,
Fu-Tsai Chiang[6] MD,
Hao-Ting Wu[3] Msc,
Lung-Fa Pan[1,3] PhD,
Lung-Kwang Pan[3] PhD

1. Department of Cardiology, Taichung Armed Forces General Hospital, Taichung 406, Taiwan; ROC,
2. Cardiovascular Center, Taichung Veterans General Hospital, Taichung 407, Taiwan; ROC,
3. Graduate Institute of Radiological Science, Central Taiwan University of Science and Technology, Takun, Taichung 406, Taiwan; ROC
4. Department of Radiation Oncology, Buddhist Tzu Chi General Hospital, Hualien 970, Taiwan, ROC
5. Department of Radiation Oncology, Yee-Zen General Hospital, Tao-Yuan 326, Taiwan, ROC
6. Department of Orthopedic Surgery, Feng Yuan Hospital, Taichung 420, Ministry of Health and Welfare, Taiwan, ROC

Keywords: Minimum detectable difference - Gamma camera - PMMA phantom - SPET scan - Student's t-test

Corresponding author:
Lung-Kwang Pan,
lkpan@ctust.edu.tw
Lung-Fa Pan,
lung-fa@803.org.tw
Graduate Institute of Radiological Science,
Central Taiwan University of Science and Technology,
Takun, Taichung 406, Taiwan; ROC

Received:
29 December 2018
Accepted revised :
24 January 2019

Abstract

Objective: An indigenous polymethyl metacrylate (PMMA) phantom with a V-shaped slit and a correlated technique for semi-quantifying the minimum detectable difference (MDD) of single photon emission tomography (SPET) via gamma camera scanning are proposed and validated using four radionuclides. **Materials and Methods:** Radio-actinide solutions of gallium-67 (^{67}Ga), technetium-99m (^{99m}Tc), iodine-131 (^{131}I) and thallium-201 (^{201}Tl) were diluted to 11c.c. and thoroughly injected into the continuous zig zag slit of the PMMA phantom. Either depth or edge of the slit between two lines of the V-shape was customized from deep or wide to change into shallow or narrow gradually. Thus, the quantified MDD could be easily evaluated, according to the revised Student's t-test evaluation. The revised Student's t-test was calculated by both full width at half maximum (FWHM) and edge width between two adjacent peaks that were acquired from the original data matrix of SPET. The derived MDD was indicated as for radionuclide, depth, width in mm: For ^{67}Ga, 2.9, 2.13, for ^{99m}Tc, 2.5, 0.66, for ^{131}I, 4.7, 2.38 and for ^{201}Tl, 3.3, 2.00, respectively. **Results:** Technetium-99m had the highest and ^{131}I had the lowest MDD among the four radionuclides. Furthermore, two adjacent peaks of ^{67}Ga could be easily identified with fewer counts than for ^{201}Tl (depth, 2.9 vs. 3.3mm), but its MDD was poorer (width: 2.13 vs.2.00mm). The revised Student's t-test analysis proved to be an acceptable technique for the MDD identification. **Conclusion:** The proposed new combination of PMMA phantom with a V-slit and the revised Student's t-test proved to be instrumental in the MDD of SPET optimization analysis.

Hell J Nucl Med 2019; 22(1): 49-57 *Epub ahead of print: 7 March 2019* *Published online: 5 April 2019*

Introduction

To maintain a high spatial resolution in single photon emission tomography (SPET) gamma camera image is always a premier task in routine quality assurance (QA) of nuclear medicine facilities. Further, the quantified minimum detectable difference (MDD) of SPET is a potent investigative tool in either clinical practice or biomedical research [1]. In most SPET clinical practices, quality assurance phantoms are usually designed either as planar lead bars [2], or as a cylindrical container with spherical balls of various diameters [3]. Both are used to provide a comparative imaging for distinguishing the artifact or lesion, since it is a complicated and challenging task to give a quantified MDD in most hospitals as a routine protocol.

Nevertheless, most optimizations of the imaging quality for gamma camera rely on the theoretical computation according to various hypotheses. For example, a filtered back-projection is still a popular adopted method for image reconstruction, which is recommended by some nuclear medicine centres [4, 5]. However, the post-processing of image reconstruction again depends on the image with bright and sharp quality characteristics in reality. Some researchers adopted the commercial phantom with a revised algorithm to develop a quantitative analysis of SPET to optimize the real imaging. For example, Zeintl et al. (2010) [6] applied a cylinder phantom to assess the performance of the reconstructed image by its consistency and reconstructed image boundaries. Mahsa et al. (2014) [7] adopted either cold-sphere/hot-background or hot-sphere/cold-background phantoms with trapezoidal and triangular approximations to evaluate the imaging quality of the derived full width at half maximum (FWHM) and claimed the scatter correction effectiveness.

Some researchers have developed indigenous phantoms compiled with an analytical method to solidify the gamma camera SPET imaging quality. For instance, Scheiber and

Giakos (2001) [8] used a customized plate phantom with multiple holes of various diameters to roughly estimate the distinguishable ability of a lesion via two commonly used semi-conductor detectors for measuring gamma rays, CdTe or CdZnTe. Yeh et al. (2013) [9] designed a planar phantom with multiple eccentric circles filled with the radioactive solution for optimizing its imaging quality through the Taguchi analysis. However, they still used a qualitative analysis. Recently, several co-authors of the present paper successfully applied the first prototype of a V-shaped water phantom to optimize the SPET image quality via the Taguchi analysis [10]. The V-shaped combination of capillaries was placed inside a cylindrical container (20cm in diameter, 30cm in height and 9 liters in volume) filled with the radioactive solution diluted to ~58% of the original radioactivity level for simulating the contrast in clinical examination.

In contrast, a newly developed phantom as introduced in this study. This phantom was designed for a convenient injection of different radioactive solutions, which is an essential requirement for clinical radiologists. The planar phantom can be scanned by a gamma camera in order to identify the actual MDD for each specific radionuclide. Such quantification is considered a top priority in optimizing the gamma camera imaging quality. Otherwise, any inappropriate judgment of the performing facility may strongly mislead the optimization. Thus, this study attempts to introduce a rapid quantitative evaluation of MDD for SPET. The proposed approach feasibility is verified by the revised Student's t-test analysis and the regular assessments of the imaging quality in real gamma scanning images.

Materials and Methods

Planar PMMA phantom with V-shaped slit

Unlike most phantoms with a lead bar pattern arrayed at various distances on a plate [11], or multiple spheres/holes of various diameters inside a cylinder [12, 13], the proposed design of a polymethyl metacrylate (PMMA) phantom with a V-shaped slit ensures a cohesion with the revised Student's t-test analysis. The zigzag array of the slit with a continuous change of slit depth provides the following gamma-ray image under scanning and, thus, the converted data matrix of SPET can be evaluated for calculating the revised Student's t-test index. Moreover, the data profile of SPET can be judged channel-by-channel to ascertain that two adjacent peaks satisfy the 95% confidence level according to definition of the revised Student's t-test after the conversion from the original gamma-ray imaging. Thus, the MDD can be quantified as precise as to one-tenth mm rather than providing an approximate value within 0.3-0.6mm range of the intrinsic spatial resolution for referring in everyday practice [11].

Unlike the original prototype of water phantom has only one V-shaped slit and difficulty to maintain its reproducibility in real scanning [10], thus, this added procedures makes the present work original. The newly Figure 1(A) shows the precise designation chart of this unique planar PMMA phantom (200×200×18mm^3). The V-shaped slit has the shallowest depth (1.0mm) at the top right corner that goes deeper along the slit to the very bottom (5.2mm). The slit width is designed as fixed 1.0mm along the pathway. It contains either seven or eight V-shaped triangles on the left and right sides, respectively. The bottom edge width varies in the following decreasing order: right bottom (167-134=33mm), left bottom (150.5-119.5=31mm), left top (24.5-17.5=7mm), right top (20-15=5mm). Accordingly, for any vertical tangent line that cuts across both sides of the triangle, one can easily assess its edge distance by the proportional principle, judging from its bottom edge and the distance to the triangular vertex, insofar as the height of each triangle is fixed at 170 mm (185-15=170mm). The unique feature of the V-shaped slit is that its top has either a narrow edge between the two lines or a shallow slit along the line to be scanned by the gamma camera. Thus, the MDD of SPET is defined by the quantification of the tangent line from the digitalized image after the SPET image conversion from the real gamma camera scans.

In contrast to the majority of commercially available planar line phantoms and test patterns, which imply a lead bar to create a hot slit/cold background [12], the V-shaped slit designed in this study provides the hot-line image with the intense-to-feeble gradation and the wide-to-narrow triangular shape for the imaging quality judgment. The phantom must be preset to be scanned at the preliminary stage. The radioactive solution is diluted to 11c.c. and dyed with blue ink for easier identification; then, it is thoroughly injected into the phantom deepest part to let the solution fill in along the V-shaped pathway for the gamma camera scanning as shown in Figure 1(B). The well-packed PMMA phantom is placed in the middle of sixteen pieces of 1-cm-thick solid water planar plates and prepared for scanning as seen in Figure 1(C); then it is scanned by the gamma camera, whereas the close-up view of the PMMA phantom and solid water planar plates altogether is depicted in Figure 1(D).

Gamma Camera/8-slice CT

This study used a gamma camera/8 slice CT (GE Discovery NM/CT 670) located at Taichung Armed Forces General Hospital, which involved an all-purpose, dual-detector, free-geometry integrated nuclear imaging camera featuring the advanced all-digital Elite NXT detector technology. It was furnished with 59 circular photomultiplier tubes (PMT) with the crystal thickness of 9.5mm inside each of the two adjustable plates (53×76mm and 6×38mm, respectively). The maximal field of view (FOV) of gamma camera could be extended to 54×40cm2±0.5mm. The auxiliary CT was preset to the spiral acquisition mode with the current voltage of 10-440mA and tube voltages of 80, 100, 120, or 140kV. The focal spot size could be switched from small (0.7×0.6) to the large one (0.9×0.9mm) and vice versa, according to the IEC0336 protocol [14].

Data collection

Four radionuclides: gallium-67 (^{67}Ga), technetium-99m (^{99m}Tc), iodine-131 (^{131}I) and thallium-201 (^{201}Tl); was adopted to evaluate the MDD of SPET, respectively in this study. The

Table 1. *The preset protocol of gamma camera to scan each specific radionuclide in this study. The scan time was preset to let the total counts reach 2.7×105. Thus, the different activity of every adopted radionuclide made no significant difference to maintain their consistency.*

Radionuclide	Activity (MBq)	Collimator	Matrix size	Energy (keV)±peak width	Total counts (count)
^{67}Ga	111	MEGP	256x256	93.0±13% 184.0±10% 300.0±10%	2.7×10^5
^{99m}Tc	740	LEGP	256×256	140.5±10%	2.7×10^5
^{131}I	37	MEGP	256×256	364.5±10%	2.7×10^5
^{201}Tl	74	LEGP	256×256	135.3±15% 167.5±10%	2.7×10^5

precise setting of the scanned protocol for gamma camera was preset at 1cm from the surface to the collimator, the collimator FOV (54×40cm^2) and other parameters are displayed in Table 1. The scanning time was defined by the total counts acquired from the real scanning, which amounted to 2.7× 105 counts. Thus, different decay activities of each particular radionuclide held a minimal difference to maintain their consistency despite the detection efficiency changes for various gamma ray energies. The energy peak width of every radionuclide was preset, according to the default one in the routine nuclear examination. In Table 1 and hereinafter, LEGP and MEGP denote the low-energy and medium-energy general purposes, respectively, of the adopted collimator [15].

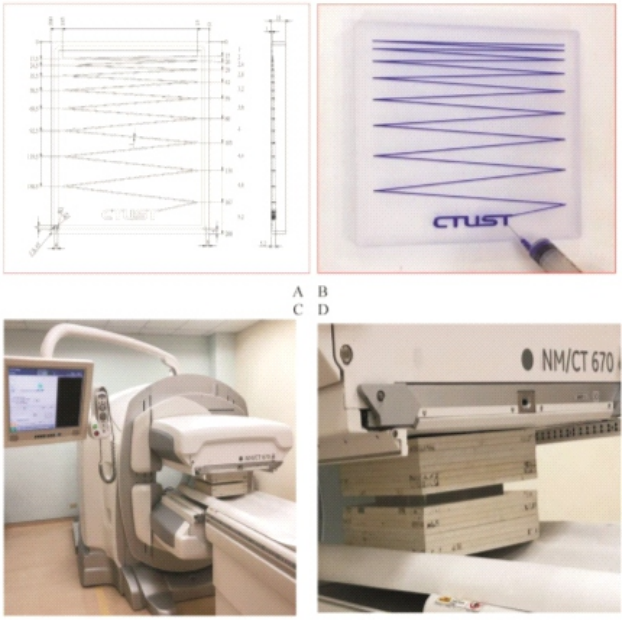

Figure 1. (A) the precise designation chart of the unique planar PMMA phantom (200×200×18mm^3). The V-shaped slit had the shallowest depth (1.0mm) at the top right corner then went deeper along the slit to the very bottom (5.2mm). The width of the slit was designed as 1.0mm along the pathway; (B) the phantom was preset to be scanned at the preliminary stage, the radioactive solution was diluted to 11c.c. and dyed with blue ink for easy recognizing; (C) the well-packed PMMA phantom was put in the middle of sixteen pieces of 1cm-thick solid water plates and prepared for scanning; (D) the close-up view of the PMMA phantom and solid water planar plates altogether.

Minimum detectable difference and revised Student's t-test analysis

Most researchers evaluate the intrinsic spatial resolution of SPET based on the individual FWHM of one peak profile. In the proposed study, the MDD of SPET is quantified from two overlapped-peak profiles acquired from a slice of the PMMA phantom with a V-shaped slit, according to the different confidence levels of success as defined by Eq. 1. In particular, it is defined as the minimum distance between two peak centers via the revised equation from the Student's t-test with the multiplied constant, 1.96, which implies that the two peak centers deviated far enough to generate a 95% confidence level of success [16]:

$$|X_1 - X_2| \geq 1.96 \times \sqrt{\left(\frac{FWHM_1}{2}\right)^2 + \left(\frac{FWHM_2}{2}\right)^2} \qquad (1)$$

Here X_1 and X_2 are the centers of peaks 1 and 2, respectively, while FWHM is the full width at half maximum of the specific peak [17]. To evaluate the MDD of SPET via the unique PMMA phantom, either the slit depth or the edge of two slits was changed gradually, to provide the quantitative assessment of its edge width and depth in its original designation. Moreover, in contrast to the first prototype of water V-phantom [10], the proposed PMMA one features a dark background/hotspot from the injected solution, which is closer to the actual clinical examination conditions. Thus, the MDD can be readily obtained, according to different confidence levels of success, as depicted in Figure 2.

A narrow FWHM is always preferable for the gamma-ray collection due to its high reproducibility of the analyzed resolution according to detector unique characteristics. As seen in Figure 2(A), two peaks can be identified as wholly separated; (B) two peaks barely passed the Student's t-test evaluation. Student's t-test is originally defined in order to identify the difference between two small groups of samples whether this difference reaches 95% confidence level. However in our revised use, we followed the same definition but replaced the theoretical standard deviation from statistical calculations by the practical measurement of the FWHM from two overlapped-peak profiles as criteria to reach the 95% confidence limit, whereas, in Figure 2(C), the two peaks are too close to be differentiated. Noteworthy is that the criteria of

passing or failing the revised Student's t-test are quantitative, since they fully depend on the calculation results, in contrast to other reports, which are based on the qualitative judgment of radiologists and may involve human factor-induced errors. Thus, the revised Student's t-test analysis may provide a more accurate and reliable evaluation of the MDD byby the quantified calculation [1, 6-10].

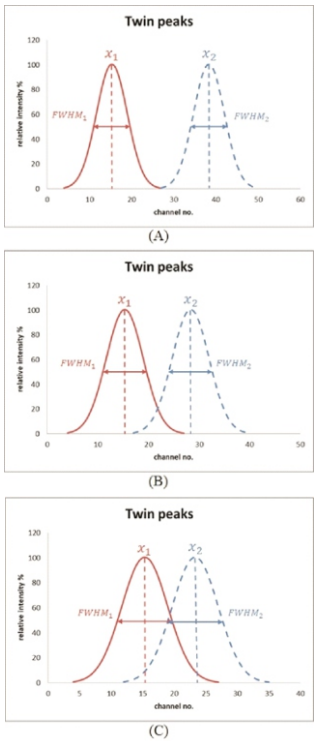

Figure 2. The MDD of SPET could be quantified from two overlapped-peak profiles; (A) two peaks were recognized as wholly separated; (B) two peaks just passed the revised t-test criterion to reach the 95% confidence level, whereas, (C) two peaks were too close to be identified as separated.

Results

Real Gamma camera imaging

Figure 3 depicts the SPET imagery of four radionuclides; (A) ^{67}Ga, (B) ^{99m}Tc, (C) ^{131}I and (D) ^{201}Tl; from the real gamma camera scanning. The data acquisition continued till the total number of counts collected within the maximal FOV of the gamma camera reached 2.7×105. Thus, various activities corresponding to different radionuclides made no significant difference from the radiological viewpoint. The quality characteristics of the SPET imaging depended only on the decay scheme of the specific radionuclide. Technetium-99m (B) had the best imaging quality characteristics and ^{131}I (C) had the worst ones, respectively. Almost every line of the PMMA phantom could be easily identified from the ^{99m}Tc SPET imaging, whereas few lines were barely distinguishable from that of ^{131}I. Insofar as the latter radionuclide is mostly administered for the ablation of thyroidectomy patients in the routine nuclear examination, the high MDD of ^{131}I SPET is not among the top priorities from the clinical standpoint.

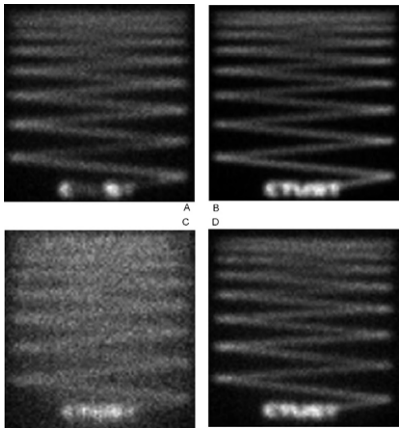

Figure 3. The imaging of four radionuclides; (A) ^{67}Ga, (B) ^{99m}Tc, (C) ^{131}I and (D) ^{201}Tl; from the real gamma camera scanning.

Conversion of gamma camera imaging results to the data matrix

The acquired SPET can be converted to data matrix [350× 350] and then plotted using the Matlab default function (/imread) for the revised Student's t-test analysis (cf. Eq. 1) [18]. The converted data matrixes of four radionuclides are depicted in Figure 4. As clearly illustrated, the color contours of scanned SPET were plotted on the left side, whereas the 3D profiles were on the right side. The MDD of the SPET for various radionuclides was explicitly defined as the critical margin for the tangent line cut across the multiple V-shaped lines, as illustrated in Figure 5. The revised Student's t-test was readily passed from the bottom part of the V-shaped two lines, and then the edge between two peaks became too small to pass the revised Student's t-test, eventually, failed to well separate two adjacent peaks (cf. Figure 2(C)). Each profile of the PMMA phantom was acquired through shifting the tangent line on the channel-by-channel basis from the right side to the left margin. As long as each pair of adjacent peaks in the same profile passed the revised Student's t-test analysis, the tangent line was shifted from one channel to the next profile for the revised Student's t-test analysis. The survey was continued with marking of the precise position in the real PMMA phantom till one pair of adjacent peaks failed the revised Student's t-test (cf. Figure 4, right side part). As clearly depicted in Figure 5, any two adjacent peaks along the tangent line were checked thoroughly by the revised Student's t-test from the acquired data profile. The plots on the left side of Figure 5 corresponding to the four radionuclides under study implied precise positions of two adjacent peaks that passed the revised Student's t-test analysis (tagged with red arrows, whereas the two adjacent peaks that failed the revised Student's t-test are plotted on the right side of Figure 5 and also marked with red arrows.

Thus, the MDD of SPET is defined as the true distance between two lines in the V-shaped slit with quantified data of width and depth that can be easily derived from the proportional principle of a similar triangle [10]. The quantified MDD of SPET is more reliable than that obtained from the reports based on the qualitative judgment of well-trained

radiologists in the hospital. Figure 6 shows the precise positions in the real PMMA phantom that passed the revised Student's t-test analysis for ^{67}Ga, ^{99m}Tc, ^{131}I and ^{201}Tl, which are marked in yellow, red, black and green colors, respectively; whereas the revised Student's t-test analysis results for the four radionuclides are listed in Table 2. Also, the corresponding MDD of SPET for various radionuclides are indicated in the first column of Table 2. Unlike the conventional evaluation of intrinsic spatial resolution, the two adjacent peaks could be precisely positioned on the V-shaped slit once the revised Student's t-test is passed. Thus, the MDD of SPET can be quantified as [nuclide, depth (mm), width (mm)]. The respective results obtained in this study are as follows: [^{67}Ga, 2.9, 2.13], [^{99m}Tc, 2.5, 0.66], [^{131}I, 4.7, 2.38] and [^{201}Tl, 3.3, 2.00].

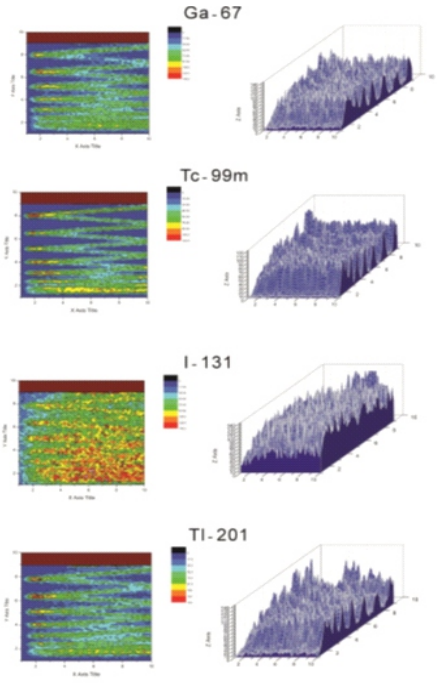

Figure 4. Left: the color contours of scanned counts for four radionuclides; right: the converted 3D profiles for the PMMA phantom with a V-shaped slit.

Discussion

MDD of SPET of four radionuclides under study

The ^{99m}Tc radionuclide has the highest MDD of SPET and ^{131}I has the lowest one among four radionuclides. In contrast, ^{201}Tl has a higher MDD of SPET (2.00mm) than ^{67}Ga (2.13mm). However, the slit depth verified for ^{201}Tl (3.3mm) is higher than that of ^{67}Ga (2.9mm). This implies that ^{67}Ga can be scanned and positioned under lower radioactivity intensity than ^{201}Tl, which can be calculated as 100%×2.9/3.3=88%, and still reliably identify two adjacent hot spots without misjudging them as a single blurred spot in the real nuclear examination. Figure 7 shows the close-up view of the SPET imaging for four radionuclides, where ^{67}Ga, ^{99m}Tc and ^{201}Tl are plotted starting from channel 0, while ^{131}I is plotted for the channel range from 100 to 150. This is done for the further cohesion of the experimental results with the calculations listed in Table 2. As seen in Figure 7, four pairs of adjacent peaks of different radionuclides are marked by different colors for their easier identification. For example, two peak centers of ^{99m}Tc are located at channels 19 and 27, respectively, with the FWHM of 5 and 6 channels. Thus, the pair of adjacent peaks passes the revised Student's t-test, according to Eq. 1 (cf. Figure 7, black line). The first peak center of ^{67}Ga is located on channel 22, whereas ^{201}Tl is on channel 29. This indicates that a lower intensity of ^{67}Ga can be identified, as compared to ^{201}Tl, although the distance between two adjacent peaks is wider (21 channels for ^{67}Ga versus 19 channels for ^{201}Tl). The MDD of SPET of ^{67}Ga is still superior to that of ^{201}Tl, judging by the complexity of the identification of two adjacent peaks. In contrast, the spectrum of ^{131}I is harder to identify. The plot in Figure 7 only partly covers the actual spectrum of ^{131}I (from channel 100 to 150). Therefore, the peak center is roughly recognized as either channel 129 or 136 for two adjacent peaks, while the MDD of SPET is 2.38mm for the 4.7mm deep slit used in this study.

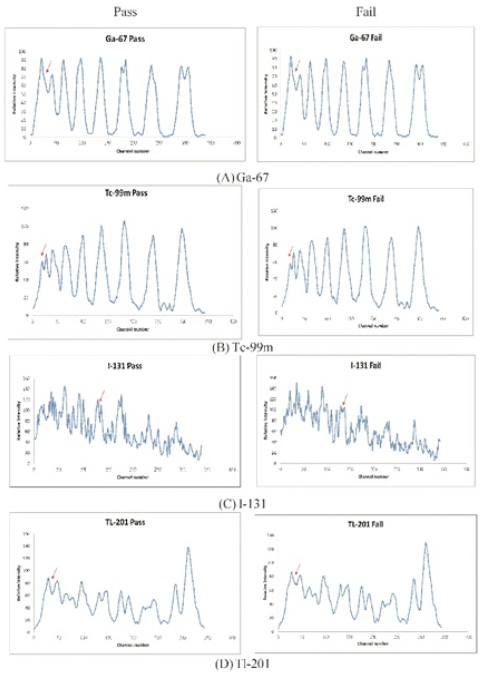

Figure 5. Any two adjacent peaks along the tangent line were checked thoroughly by the revised Student's t-test from the acquired data profile. The left side of the four radionuclides implied precise positions of two adjacent peaks that passed the revised Student's t-test analysis and tagged with a red arrow, whereas the two adjacent peaks that failed the revised Student's t-test are shown on the right side with the red arrow too.

Figure 6. The precise positions of the real V-shaped phantom that passed the revised Student's t-test analysis. ^{67}Ga, ^{99m}Tc, ^{131}I and ^{201}Tl were marked in yellow, red, black and green colors, respectively.

Table 2. *The precise calculation of the revised Student's t-test for four radionuclides, the left side show the two adjacent peaks that passed the revised Student's t-test, whereas the right side failed the revised Student's t-test.*

MDD (mm)	$\lvert X_1 - X_2\rvert \geq 1.96 \times \sqrt{\left(\frac{FWHM_1}{2}\right)^2 + \left(\frac{FWHM_2}{2}\right)^2}$	
	Pass	Fail
^{67}Ga Depth:2.9 Width:2.13	$\lvert 22-43\rvert \geq 1.96 \times \sqrt{\left(\frac{13}{2}\right)^2 + \left(\frac{15}{2}\right)^2}$ $\lvert -21\rvert \geq 1.96 \times \sqrt{56.25+42.25}$ $21 \geq 19.45$	$\lvert 22.5-42.5\rvert \geq 1.96 \times \sqrt{\left(\frac{17}{2}\right)^2 + \left(\frac{15}{2}\right)^2}$ $\lvert -20\rvert \geq 1.96 \times \sqrt{72.25+56.25}$ $20 \leqq 22.2$
^{99m}Tc Depth:2.5 Width:0.66	$\lvert 19-27\rvert \geq 1.96 \times \sqrt{\left(\frac{5}{2}\right)^2 + \left(\frac{6}{2}\right)^2}$ $\lvert -8\rvert \geq 1.96 \times \sqrt{6.25+9}$ $8 \geq 7.65$	$\lvert 18-26\rvert \geq 1.96 \times \sqrt{\left(\frac{6}{2}\right)^2 + \left(\frac{8}{2}\right)^2}$ $\lvert -8\rvert \geq 1.96 \times \sqrt{9+16}$ $8 \leqq 9.8$
^{131}I Depth:4.7 Width:2.38	$\lvert 129-136\rvert \geq 1.96 \times \sqrt{\left(\frac{3}{2}\right)^2 + \left(\frac{6}{2}\right)^2}$ $\lvert -7\rvert \geq 1.96 \times \sqrt{2.25+9}$ $7 \geq 6.57$	$\lvert 134-138\rvert \geq 1.96 \times \sqrt{\left(\frac{4}{2}\right)^2 + \left(\frac{2}{2}\right)^2}$ $\lvert -4\rvert \geq 1.96 \times \sqrt{4+1}$ $4 \leqq 4.38$
^{201}Tl Depth:3.3 Width:2.00	$\lvert 29-48\rvert \geq 1.96 \times \sqrt{\left(\frac{13}{2}\right)^2 + \left(\frac{14}{2}\right)^2}$ $\lvert -19\rvert \geq 1.96 \times \sqrt{42.25+49}$ $19 \geq 18.7$	$\lvert 29-47\rvert \geq 1.96 \times \sqrt{\left(\frac{14}{2}\right)^2 + \left(\frac{13}{2}\right)^2}$ $\lvert -18\rvert \geq 1.96 \times \sqrt{49+42.25}$ $18 \leqq 18.72$

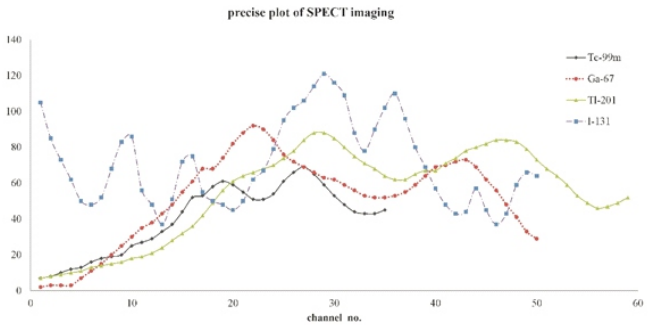

Figure 7. Four pairs of adjacent peaks of different radionuclides were marked by different colors for easy differentiation: ^{99m}Tc in black, ^{67}Ga in red, ^{201}Tl in green, and ^{131}I in blue.

The advantages of MDD over FWHM of SPET

In contrast, the conventional definition of intrinsic spatial resolution of SPET [10], the MDD of SPET used in this study is more focused on the identification of two adjacent peaks that are separated and confirmed over the 95%-confidence level. As seen in Table 3, FWHM for either peak 1 or 2 has fewer channels than the actual number of channels between the center of peaks 1 and 2 for the four radionuclides under study. This is because that the preset confidence level for providing an excellent recognizing ability is 95% or higher. Thus, two peaks need to be distinctly separated to satisfy the criterion of MDD of SPET. For example, for ^{67}Ga radionuclide, FWHM amounts to either 13 or 15 channels, whereas that between two peaks centers has to reach 21 to pass the revised Student's t-test. Furthermore, it is implied as 2.13mm at the 2.9mm-deep slit in the actual PMMA phantom, according to the triangle proportional principle. The similar pattern for the remaining three radionuclides listed in Table 3 reveals that the revised Student's t-test is more instrumental than the conventional definition of the intrinsic spatial resolution for SPET. It is beneficial to determine the difference between two adjacent peaks rather than to represent an isolated peak with narrow FWHM in SPET. Nevertheless, the revised Student's t-test analysis compiles three essential variables, namely, two FWHM values of two adjacent peaks, and the distance between two peak centers. Moreover, the revised Student's t-test analysis is more applicable to practical situations in the clinical diagnosis than the conventional intrinsic spatial resolution defined only by a single peak of SPET. For example, as clearly depicts in Figure 8, the high MDD of SPET can effectively intensify diagnosis of deep vein thrombosis (DVT) syndrome for patient undergone ^{99m}Tc-MAA venography examination The precise distribution of posterior/anteri-

Table 4. *The essential information of derived FWHM or MDD quoted from previous contributions and this study as well.*

Ref.	Radionuclide	Given activity (MBq)	Source pattern	Collimator	The distance from the surface to the collimator (mm)	FWHM (mm)	MDD (mm)
[6]	^{99m}Tc	N/A	Voxel size 0.66mm	LEHR	100	7.4	
[11]	^{57}Co	N/A	0.3mm slit	1-mm pinhole	10	~0.6	
[19]	^{99m}Tc	2.18	Line source	1-mm pinhole	30	2.8	
[20]	^{99m}Tc	1.1	Quadrant bar phantom	No	N/A	4.5-5.2	
[21]	^{22}Na	N/A	0.3mm point	N/A	N/A	1.81	
[22]	^{99m}Tc	37	0.03mm slit	2-mm pinhole	28	0.34	
	^{125}I	37				0.27	
[23]	^{99m}Tc	1.85	1mm slit	LEHR	100	14.4	
This study							
	^{67}Ga	111	PMMA phantom with 1.0mm V-shaped slit	MEGP	80	1.00, 1.14	2.13
	^{99m}Tc	740		LEGP		0.41, 0.50	0.66
	^{131}I	37		MEGP		1.02, 2.04	2.38
	^{201}Tl	74		LEGP		1.37, 1.47	2.00

or tibial veins can be easily identified via an optimal preset of gamma camera imaging acquiring system [9, 10].

Table 3. *The channel and corresponded real edge width or slit depth in the unit of mm for two adjacent peaks that pass the revised Student's t-test in this study.*

	P_1 (FWHM) channel/mm	P_2 (FWHM) channel /mm	P_1-P_2 channel /mm	depth (mm)
^{67}Ga	13/1.00	15/1.14	21/2.13	2.9
^{99m}Tc	5/0.41	6/0.50	8/0.66	2.5
^{131}I	3/1.02	6/2.04	7/2.38	4.7
^{201}Tl	13/1.37	14/1.47	19/2.00	3.3

The definition of a revised Student's t-test can also be simplified by omitting the constant equal to 1.96 in Eq. (1) calculation. However, this simplification may result in the confidence level reduction to 68%, which would be detrimental for the proposed method reliability. For the comparative analysis of the gamma camera FWHM or MDD of SPET obtained in similar studies, the detailed information from relevant reports is compiled in Table 4. As depicted, a precise FWHM is controlled by two factors: radioactive source pattern and unique designed collimator. For example, fine source pattern (with either 0.3 or 0.03mm slit) can eventually yield FWHM of 0.27-1.81mm via 1- or 2mm pinhole [11, 21, 22]. The results were mostly obtained from either theoretical simulation or academic research. However, only a few of those reports were focused on the distinguishable ability of two correlated spots on the scanned imaging from a practical survey. In contrast, the dominant feature of gamma camera scanning in a clinical nuclear examination is to identify the distribution of the administered radionuclide solution or

to inspect the metabolic mechanism, according to the derived biokinetic model of patients. Thus, a high MDD can effectively ascertaining the lesion or artifacts from a clinical viewpoint.

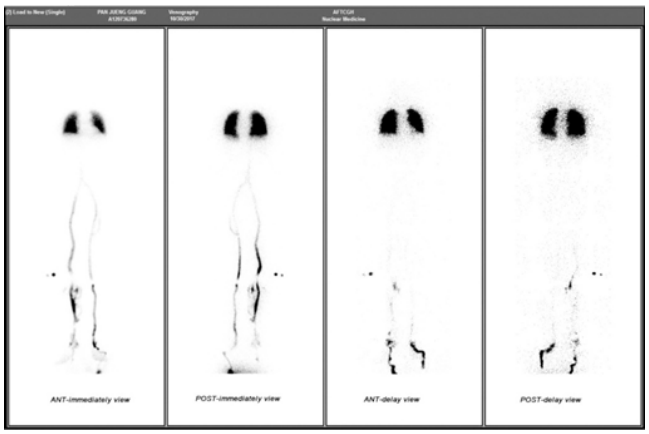

Figure 8. Patient undergone ^{99m}Tc-MAA venography examination with significant deep vein thrombosis (DVT) syndrome. The precise distribution of posterior/anterior tibial veins can be easily identified via an optimal preset of gamma camera imaging acquisition system

To effectively apply the proposed PMMA phantom, the protocol of gamma camera scanning should be set into the scan-and-stop mode by acquiring the gross count to a fixed amount (ex. 2.7×105 in this study). This figure is appropriate for practical measurements, insofar as too long or too short counting time may (1) cause too dark or too light background of all gamma-ray images that would interfere with the post-analysis of SPET; (2) mislead the real gamma spectrum performance. Since each radionuclide has its unique decay gamma-ray spectrum, the detection efficiency is also changed in the actual measurements. Either excessive or insufficient counting time may promote the Compton scattering to interfere the main peak of the specific gamma-ray, whereas the gamma camera scan-and-stop mode acquired by presetting gross counts can suppress all potential uncertainties and result in a uniform distribution of the radio-actinide solution along the zigzag path with assigned gross counts. This is essential to minimize the intrinsic interfering in real scanning.

In conclusion, an indigenous PMMA phantom with a V-shaped slit and correlated technique for quantifying the minimum detectable difference (MDD) of single photon emission tomography (SPET) of four radionuclides (^{67}Ga, ^{99m}Tc, ^{131}I and ^{201}Tl) via the gamma camera scanning was proposed in this study. The unique designation of the proposed PMMA phantom allows one to efficiently evaluate the MDD of SPET and provide the quantified information for the comparative analysis. Accordingly, ^{99m}Tc and ^{131}I had the highest and lowest MDD among the four radionuclides under study, whereas ^{67}Ga or ^{201}Tl had the optimal imaging characteristics in identifying two adjacent peaks with shallow or narrow slits. The design of the newly developed planar PMMA phantom implies a gradual variation of the slit depth, which yields more reliable quantitative assessment of its width and depth. This feature makes it lucrative for the quantitative analysis of MDD for SPET imaging of gamma camera. Thus, the proposed new combination of PMMA phantom with a V-slit and the revised Student's t-test proved to be instrumental in the MDD of SPET optimization analysis.

Acknowledgment

The authors would like to thank the National Defense-Medical Affairs Bureau under contract No. ND 107-A25 and the Ministry of Science and Technology of the Republic of China under contract No. MOST 106-2221-E-166-002 for the financial support of this research.

The authors declare that they have no conflicts of interest.

Bibliography

1. Bailey DL, Willowson KP. An evidence-based review of quantitative SPECT imaging and potential clinical applications. *J Nucl Med* 2013; 54: 83-9.
2. Gamma camera bar phantom and test pattern, Fluke Biomedical, http://www.flukebiomedical.com/biomedical/usen/nuclear-medicine/quality-control-phantoms/76-890-ub-gamma-camera-test-pattern.htm?pid=55297
3. Jaszczak SPECT Phantom, scannix, https://www.scannix.com/produit/jaszczak-spect-phantom/.
4. Parker JA, Daube-Witherspoon ME, Graham LS et al. Society of Nuclear Medicine Procedure Guideline for General Imaging. Reston, VA: The Society of Nuclear Medicine; 2004. Available at: http://interactive.snm.org/docs/General_Imaging_v3.0.pdf. Accessed April 21, 2010.
5. Hesse B, Taegil K, Cuocolo A et al. EANM/ESC procedural guidelines for myocardial perfusion imaging in nuclear cardiology. *Eur J Nucl Med Mol Imaging* 2005; 32: 855-97.
6. Zeintl J, Vija AH, Yahil A et al. Quantitative Accuracy of Clinical ^{99m}Tc SPECT/CT Using Ordered-Subset Expectation Maximization with 3-Dimensional Resolution Recovery, Attenuation, and Scatter Correction. *J Nucl Med* 2010; 51: 921-8.
7. Mahsa NA, Alireza S, Ahmad BR. Evaluation of three scatter correction methods based on estimation of photopeak scatter spectrum in SPECT imaging: A simulation study. *Physica Medica* 2014; 30: 947-53.
8. Scheiber C, Giakos GC. Medical applications of CdTe and CdZnTe detectors. *Nucl. Instruments & Methods in Phys Res. A* 2001; 458: 12-25.
9. Yeh DM, Chang PJ, Pan LK. The optimum Ga-67-citrate gamma camera imaging quality factors as first calculated and shown by the Taguchi's analysis. *Hell J Nucl Med* 2013; 16(1): 25-32.
10. Kittipayak S, Pan LF, Chiang FT et al. The Optimization of the Single Photon Emission Computed Tomography Image Quality via Taguchi Analysis: A Feasibility Study of a V-Shaped Phantom. *J Med Imag Health Inform* 2017; 7(1): 143-8.
11. Nakanishi K, Yamamoto S, Kataoka J. Performance comparison of finely channeled LYSO-and GAGG-based Si-PM gamma cameras for high-resolution SPECT. *NIMA A* 2017; 872: 107-11.
12. Noori-Asl M, Sadremomtaz A, Bitarafan-Rajabi A. Evaluation of three scatter correction methods based on the estimation of photopeak scatter spectrum in SPECT imaging: A simulation study. *Physica Medica* 2014; 30: 947-53.
13. Scheiber C, Giakos GC. Medical applications of CdTe and CdZnTe detectors. *NIMA A* 2001; 458: 12-25.
14. GE Discovery NM/CT 670 technical report, https://mind.net.au/wp-content/uploads/2017/01/ Discovery-NMCT-670-Pro-Data-Sheet.pdf
15. Cherry SR, Sorenson JA, Phelps ME. Physics in Nuclear Medicine, 4th edn Saunders, Elsevier. ISBN: 978-1-4160-5198-5.
16. Kenny DA, Mannetti L, Pierro A et al. The Statistical Analysis of Data From Small Groups. *J Personal Soc Psychol* 2002; 83(1): 126-37.
17. Turner JE. Atoms, Radiation, and Radiation Protection, 2nd edn John Wiley & Sons, Inc. 2000. ISBN 978-3-527-40606-7.
18. MATLAB. Matrix laboratory developed by MathWorks. V7.0.1.24704 (R14) (2004) http://www.mathworks.com/products/matlab/whatsnew.html.

19. Zeniya T, Watabe H, Aoi T et al. Use of a compact pixellated gamma camera for small animal pinhole SPECT imaging. *Annal of Nucl Med* 2006; 20(6): 409-16.
20. Alkhorayef MA, Alnaaimi MA, Alduaij MA et al. Toward standardising gamma camera quality control procedures. *Radiation Phys And Chem* 2015; 116: 95-9.
21. Islami rad SZ, Gholipour Peyvandi R, Askari Lehdarboni M et al. Design and performance evaluation of a high resolution IRI-microPET preclinical scanner. *NIMA A* 2015; 781: 6-13.
22. Beekman FJ, Vree GA. Photon-counting versus an integrating CCD-based gamma camera: important consequences for spatial resolution. *Physics in Med and Biol* 2005; 50: N109-N119.
23. Velo P, Zakaria A. Determining Spatial Resolution of Gamma Cameras Using MATLAB. *J Med Imag Radiat Scienc* 2017; 48: 39-42.

Unknown artist of the second half of the 18th century. Portrait of Catherine II the Great (1729-1796), Empress of Russia in a travelling dress.